

# IGRF-14 GFZ candidates

M. Rother<sup>1</sup>, I. Michaelis<sup>1</sup>, M. Schanner<sup>1,2</sup>, M. Korte<sup>1</sup>, J. Matzka<sup>1</sup>,  
M.V.S. da Silva<sup>1</sup>

September 29, 2024

<sup>1</sup> Helmholtz Centre Potsdam, GFZ German Research Centre for Geosciences, Telegrafenberg, 14473 Potsdam, Germany.

<sup>2</sup> Applied Mathematics, Postdam University, Germany

## 1 Introduction

This document outlines technical details of the creation of the GFZ candidates for the IGRF-14, in particular the estimation of the parent `Mag.num` models. A brief description of the outcome is included as well. First, an outline of the general (classic) approach is presented. This approach is used to generate 20 parent models, from which the candidates are derived. Later sections describe more detailed aspects of the three delivered candidate types (`DGRF`, `IGRF` and `SV`).

The procedure of the parent `Mag.num` modelling is in its core the same as for the GFZ IGRF-12 and GFZ IGRF-13 candidate submissions. Most of the fundamental descriptions apply to the `Mag.num` parent modelling as well. We follow closely the technical description of the IGRF-12 and IGRF-13 candidate [Lesur *et al.*, 2014]. After a decade of Swarm operation, the outer modelling flow has changed, on one hand due to the mere amount of data, and on the other hand some details of data selection, filtering and preparation have changed. The long reference `Mag.num` model (with nodes from 2000 - 2025) is based on additional satellite data sources: on the CHAMP data (version L3), and on ex post in-flight calibrated GOCE and CryoSat satellite data, in particular to cover the data gap.

In addition to the long model, shorter models (with nodes 2013 - 2025) are part of our IGRF-14 candidate. These models cover the Swarm era (selected data from the 1 Hz `SW_OPER_MAGB_LR_1B` product) – as they are known to be very well-formed and of low noise – and are also built on the corresponding harmonised and selected observatory hourly means data, delivered as the Swarm `AUX_OBS` product by BGS [Macmillan and Olsen, 2013].

Both epochs, 2020 for the `DGRF` and a major part of 2024, are covered by processed and calibrated Swarm magnetic vector field readings. Therefore, the parent model for the `DGRF 2020` and `IGRF 2025` use the same Swarm data and the description in Section 2 (`DGRF 2020`) applies to `IGRF 2025` as well, if not stated otherwise.

Other satellite (GOCE, CryoSat, CHAMP) and observatory sources do not undergo further adaptation (e.g. Euler angles) and are, aside from the crucial data selection, used from

the available source locations **as is** and use the `NEC` system as input, without additional rotation, e.g. from the satellite system.

## 2 General technical description

### 2.1 Data

One of the `Mag.num` parent model inputs are Swarm satellite data, taken from the `SW_OPER_MAGB_LR_1B`; 1 Hz vector field readings for all three satellites in the `MJD2000` time period 5077 - 8995, which is 2013-11-27 - 2024-08-16 as civil date. The Swarm data versions are of baseline 06 with versions 02 till 06.

The input hourly means of the `AUX_OBS` Swarm product portfolio are of baseline 01 and version 20, copied from the `ftp.nerc-murchison.ac.uk` server in August 2019. The time coverage of the various observatories may differ significantly, last observatory entries are of July 2019.

For the long period `Mag.num` model the following additional satellite data sources are used:

**CHAMP L3 data:** Final calibrated, Level 3 `LEO` satellite `CHAMP` data, one Hz (*Rother and Michaelis [2019]*).

**CryoSat :** Inflight calibrated platform magnetometer from CyroSat satellite (*Olsen et al. [2020]*).

**GOCE:** Inflight calibrated platform magnetometer from GOCE satellite (*Styp-Rekowski et al. [2022]*).

Input data from `SWARM` are magnetic field vector data in the sensor system. For the rotation from sensor system into the target systems of the vector field data, the corresponding attitude data are used. A set of Euler angles for a bin-wise constant time-dependent correction is co-estimated, as soon as the core model field and the external field parameters seem to be appropriately stable.

### 2.2 Selection

#### 2.2.1 Satellite data

The selection criteria used for these data are very similar to those used in the `GRIMM` series of models [*Lesur et al., 2008, 2010; Mandeia et al., 2012*], the `DCO` (Dedicated Core) Swarm `L2` product and the previous `GFZ IGRF-13` candidate model.

The considered equatorial vector data, i.e. between  $\pm 55^\circ$  magnetic latitude for magnetically quiet times, are rotated into the `SM` coordinate system. Polar data ( $> |55^\circ|$ ) are not rotated.

The following criteria are applied to select used data sets:

- Positive value of the  $z$ -component of the interplanetary magnetic field ( $\text{IMF-}B_z$ ).

- The minimal time between sampled points is set to 20 seconds.
- Data are selected only at local times between 23:00 and 05:00.
- For the special task of Euler estimation only this limit is extended to 18:00 to 06:00 local time.
- Data are selected only when the sun is below the horizon at 100 *km* above the Earth's reference radius of 6371.2 km.
- As external field index, the `MMA_SHA_2F` Swarm Level 2 product is used for the Swarm era. The thresholds for the values and their time derivatives vary, as during the modeling process some re-selections are done with slightly tightened limits, partly to try to reduce noise, partly to reduce the data load.
- Quality flags are used to select periods with acceptably accurate satellite positioning and star cameras quality. The chosen limits are heuristic and have not been changed after the long phase of `DCO` modelling.

In polar regions, pole-wards of  $|55^\circ|$  of magnetic latitude, the `ECEF` North, East, Centre (`NEC`) system is used for the vector magnetic field data.

For this polar region data, the selection criteria of the local time window and the sun position are dropped.

### 2.2.2 Observatory data

Very similar criteria are applied for the selection of the observatory data, but the `Dst` index is (traditionally) used for the parameterisation of the external field.

Some observatories are dropped entirely, but mostly a threshold controlled outlier removal was applied after a sequence of first model iterations, as soon as the individual observatory offsets and all other external field parameters appear to be settled. No outlier-neighbourhood removal (as for the satellite data) was applied.

## 2.3 Weights

The weights are a modified versions of the Huber weights. The weights  $w_j$  calculated from a given data value  $d_j$ , a set of model parameters  $\mathbf{g}$  and a sensitivity matrix  $\mathbf{A}$ , are given in equation 1. The prior data standard deviation  $\sigma_j$ , and the scalar  $k_j$  and  $a_j$  are given in the table 2. If  $\mathbf{g}$  is not given,  $w_j = \frac{1}{\sigma_j}$ .

$$w_j = \begin{cases} \frac{1}{\sigma_j} & \text{for } |d_j - \mathbf{A}_j \cdot \mathbf{g}| \leq k_j, \\ \frac{1}{\sigma_j} \left[ \frac{k_j}{|d_j - \mathbf{A}_j \cdot \mathbf{g}|} \right]^{1 - \frac{a_j}{2}} & \text{for } |d_j - \mathbf{A}_j \cdot \mathbf{g}| > k_j, \end{cases} \quad (1)$$

There is an additional iterative process of outlier removal. Far outliers are removed after first iterations together with their neighbourhood (approx a few minutes), assuming that distortions mostly come in bursts. When the residuals decrease, due to improved external field estimation and increased validity of the model fit, the hard thresholds are tightened

slightly. Only a few percent of the data are removed by this scheme. Equatorial and polar data are handled separately.

There is a large difference for the polar data between the X,Y and the Z component. The final threshold for X and Y is about  $\pm 300\text{nT}$ , the threshold for Z is much smaller (of about  $\pm 100\text{nT}$ ).

## 2.4 Model

Away from its sources, the magnetic field can be described as the negative gradient of potentials associated with sources of internal and external origin:

$$\begin{aligned} \mathbf{B} &= -\nabla\{V_i(\theta, \phi, r, t) + V_e(\theta, \phi, r, t)\} \\ V_i(\theta, \phi, r, t) &= a \sum_{l=1}^{L_i} \sum_{m=-l}^l \left(\frac{a}{r}\right)^{l+1} g_l^m(t) Y_l^m(\theta, \phi) \\ V_e(\theta, \phi, r, t) &= a \sum_{l=1}^{L_e} \sum_{m=-l}^l \left(\frac{r}{a}\right)^l q_l^m(t) Y_l^m(\theta, \phi) \end{aligned} \quad (2)$$

where  $Y_l^m(\theta, \phi)$  are the Schmidt semi-normalized spherical harmonics (SHs).  $\theta, \phi, r$  and  $a$  are the co-latitude, longitude, satellite altitude and model reference radius, respectively, in geocentric coordinates. We use the convention that negative orders,  $m < 0$ , are associated with  $\sin(|m|\phi)$  terms whereas null or positive orders,  $m \geq 0$ , are associated with  $\cos(m\phi)$  terms.

For the largest wavelengths of the field generated in the core and lithosphere (here, assumed up to SH degree  $L_i = 18$ ), the reference radius used in equation (2) is  $a = 3485 \text{ km}$ . The Gauss coefficients are parameterised in time from 2013 to 2020, using order six B-splines  $\psi_i^6(t)$ , with half-year time intervals between the spline nodes. Therefore, the time dependence of the Gauss coefficients is given by:

$$g_l^m(t) = \sum_{j=1}^{N_t} g_{lj}^m \psi_j^6(t), \quad (3)$$

where  $N_t = 9$ . For the core and lithospheric field of SH degree greater than 18, the reference radius is set to  $a = 6371.2 \text{ km}$ . The maximum SH degree used for modelling the field of internal origin is 30, although a time-invariant field covering all SH degrees from 25 to 80 is subtracted from the data so that only very small contributions from the lithospheric field remain unmodelled. The remaining parts of the internal field are the induced fields that are modelled using only one coefficient, for  $N_e = 4$  different 6-month time intervals, scaling the internal part of the  $Dst$  index – i.e. the  $Dst_i$ . The time dependence of the Gauss coefficient  $g_1^0(t)$  is therefore modified to:

$$g_1^0(t) = \sum_{j=1}^{N_t} g_{1j}^0 \psi_j^6(t) + \sum_{j=1}^{N_e} g_{1j}^{0Dst} \mathcal{H}_j(Dst_i), \quad (4)$$

where the function  $\mathcal{H}_j(X)$  takes the value  $X$  in the time interval  $[t_j : t_{j+1}]$  and is zero otherwise. For observatory data we also co-estimate crustal offsets.

The external field parameterisation also consists of independent parts. A slowly varying part of the external field model is parameterised over each 6-month time interval by a

degree  $l = 1$  order  $m = 0$  coefficient in the Geocentric Solar Magnetic (GSM) system of coordinates, and two coefficients of SH degree  $l = 1$ , with orders  $m = 0$  and  $m = -1$  in a Solar Magnetic (SM) system of coordinates. The rapidly varying part of the external field is controlled using the external part of the  $Dst$  index – i.e. the  $Dst_e$ , and the  $IMF \mathbf{B}_y$  time series. Here again 6-month time intervals are used. Four scaling coefficients for the  $Dst_e$  are introduced in each interval: three for SH degree  $l = 1$  and orders  $m = -1, 0, 1$  and one for SH degree  $l = 2$  and order  $m = 0$ . One scaling coefficient for the  $IMF \mathbf{B}_y$  is introduced in each time interval for SH degree  $l = 1$  and order  $m = -1$  in SM system of coordinates. Overall, the parameterisation of the external field is:

$$\begin{aligned}
\mathbf{B}_e(\theta, \phi, r, t) = & \\
& -\mathcal{R}_{GSM} \quad \nabla \quad \left[ \quad r \sum_{j=1}^{N_e} \{ q_{1j}^{0GSM} Y_1^0(\theta, \phi) \} \mathcal{H}_j(1) \right] \\
& -\mathcal{R}_{SM} \quad \nabla \quad \left[ \quad r \sum_{j=1}^{N_e} \{ q_{1j}^{0SM} Y_1^0(\theta, \phi) + q_{1j}^{-1SM} Y_1^{-1}(\theta, \phi) \} \mathcal{H}_j(1) \right] \\
& -\nabla \quad \left[ \quad r \sum_{j=1}^{N_e} \left\{ \sum_{m=-1}^1 q_{1j}^m Dst Y_1^m(\theta, \phi) + \left(\frac{r}{a}\right) q_{2j}^0 Dst Y_2^0(\theta, \phi) \right\} \mathcal{H}_j(Dst_e) \right] \\
& -\mathcal{R}_{SM} \quad \nabla \quad \left[ \quad r \sum_{j=1}^{N_e} \{ q_{1j}^{-1IMF} Y_1^{-1}(\theta, \phi) \} \mathcal{H}_j(IMF \mathbf{B}_y) \right]
\end{aligned} \tag{5}$$

where  $\mathcal{R}_{GSM}$  and  $\mathcal{R}_{SM}$  are matrices rotating vectors defined in GSM and SM reference frames into the geocentric Earth fixed reference frame, respectively.

We used independent external field parameterisations for the satellite and observatory data. In the latter, we impose that  $q_{1j}^{0SM}$  is set to zero to avoid co-linearities with the observatory crustal offsets.

## 2.5 Process

The solution is obtained after several iterations of an Iterative Re-weighted Least-Squares scheme where the square root values of the weights are given by equation 2.

The uniformity of the fit, i.e. the behaviour of the residuals as function of time is checked after some iterations. A new setup after re-run a re-tuned selection process can be necessary.

### 2.5.1 Using differences

In addition to the inversion based on single vector magnetic field data, `Mag.num` versions based only on Swarm difference data (along and cross track) are created. For this data set, only a small amount of damping is required and no external field estimation is done. It turns out that this data set allows a simple estimation of the secular variation but leads to inaccurate estimation of the magnetic field coefficients of low degree. The comparison to observatory data and to other models shows a good fit (the comparison to other models is not shown in this document).

One of this 'Delta'-model versions of the `Mag.num` model was used as a starting model for the short classic `Mag.num` candidate parent versions.

## 2.6 Euler Angles

The rotation angles between magnetic field vectors in the sensor reference frame and the satellite coordinated system are estimated as constants in fixed time intervals, as presented in *Rother et al.* [2013]. The size of the bins in days is usually modified during the iterative process. For the `Mag.num` parent models (short and long) the bin-size is 17 days. No estimation is done for a bin, if the bin population number drops below 1000, which is usually caused by gaps.

## 2.7 Regularisation

Regularisation is only applied to the part of the temporally varying core field. The long period parent model is intentionally **not** very stiff, i.e. only weak regularisation is applied. For both model types, short and long ones, the third derivative is moderately damped, while secular variation and acceleration are only damped at the first and last node. The (guessed) initial values for the damping parameters are adapted during further iterations to avoid obviously unphysical behaviour, but no (rigorous) algorithm is applied.

Table 1: Satellite used data numbers and limits of the periods covered, split by satellite sources; CryoSat and GOCE data are limited to cover and overlap the gap between the CHAMP and Swarm data sets as good as possible.

Source	nr. of vectors equatorial in 1	nr. of vectors polar in 1	MJD2000 start day	MJD2000 end day
Swarm A	522442	1424441	5077	8995
Swarm B	482590	1425109	5077	8995
Swarm C	522843	1428871	5077	8995
CHAMP	657282	1234576	211	3899
CryoSat	604011	924978	3867	5476
GOCE	216311	489240	3592	5021

Table 2: Satellite and observatory bias and sigmas of the last iteration of the long period `Mag.num` parent model, the first row shows the data type... `[1, 2, 3]` are the mid- and low-latitude X, Y and Z satellite data in SM, `[11, 12, 13]` are high-latitude satellite (Swarm) data.  $N$  is designating the number of data values,  $\sigma$  the standard deviation in nT. The negative type identifier numbers `[-1, -2, -3]` are additional data in a slightly extended local time window, but exclusively used for the Euler angle estimation.

Type	Type	Number	Bias	Sigma
in 1		(components) in 1	in nT	in nT
Sat				
1	X equ.	3005479	0.022	9.180
-1		1750389	0.179	3.412
2	Y equ.	3005479	-0.041	5.263
-2		1750389	0.070	3.185
3	Z equ.	3005479	0.357	7.597
-3		1750389	-0.859	4.125
11	X pol.	6927215	-0.109	42.435
-11		492	0.192	7.444
12	Y pol.	6927215	0.411	49.748
-12		492	-1.713	7.928
13	Z pol.	6927215	0.082	16.844
-13		492	0.066	5.578
Obs				
6	X equ.	1980344	0.142	4.625
7	Y equ.	1980344	-0.091	4.836
8	Z equ.	1980344	-0.001	6.652
16	X pol.	553883	0.030	31.872
17	Y pol.	553883	0.034	17.139
18	Z pol.	553883	0.025	28.204

Table 3: As there are satellite sources beside Swarm A, B and C, the statistics of the last iteration for the long period Mag.num parent model are specified here, but as result of the R standard `boxplot` command, which applied an internal outlier detection beforehand. The corresponding figure is Fig.1. As usual, the values for the sources are split by components and into the equatorial and polar region.

Type	Source	Lower Whisker in nT	Lower Hinge in nT	Median in nT	Upper Hinge in nT	Upper Whisker in nT
X equ.	Swarm A	-6.889	-1.669	0.027	1.811	7.031
X equ.	Swarm B	-6.832	-1.555	0.180	1.963	7.239
X equ.	Swarm C	-7.153	-1.814	-0.068	1.746	7.085
X equ.	CHAMP	-7.327	-1.847	-0.026	1.807	7.287
X equ.	CryoSat	-11.416	-2.869	-0.020	2.828	11.374
X equ.	GOCE	-18.441	-4.663	-0.120	4.523	18.300
Y equ.	Swarm A	-6.730	-1.812	-0.186	1.468	6.386
Y equ.	Swarm B	-6.328	-1.513	0.076	1.698	6.513
Y equ.	Swarm C	-6.785	-1.792	-0.122	1.539	6.534
Y equ.	CHAMP	-6.663	-1.640	0.026	1.708	6.731
Y equ.	CryoSat	-9.487	-2.366	-0.008	2.381	9.501
Y equ.	GOCE	-19.687	-5.065	-0.187	4.684	19.308
Z equ.	Swarm A	-7.375	-1.593	0.328	2.261	8.042
Z equ.	Swarm B	-7.118	-1.534	0.313	2.189	7.773
Z equ.	Swarm C	-7.294	-1.521	0.393	2.327	8.100
Z equ.	CHAMP	-9.681	-2.126	0.384	2.911	10.465
Z equ.	CryoSat	-16.385	-3.960	0.242	4.323	16.747
Z equ.	GOCE	-20.507	-4.661	0.654	5.903	21.742
X pol.	Swarm A	-40.558	-10.026	0.546	10.329	40.861
X pol.	Swarm B	-39.986	-9.805	0.564	10.316	40.498
X pol.	Swarm C	-40.840	-10.092	0.579	10.407	41.156
X pol.	CHAMP	-38.246	-8.997	0.653	10.503	39.752
X pol.	CryoSat	-39.243	-9.445	0.645	10.420	40.217
X pol.	GOCE	-46.662	-11.476	0.474	11.982	47.169
Y pol.	Swarm A	-42.598	-10.298	0.177	11.235	43.535
Y pol.	Swarm B	-42.895	-10.538	0.049	11.034	43.392
Y pol.	Swarm C	-42.896	-10.398	0.117	11.268	43.766
Y pol.	CHAMP	-39.395	-9.720	0.023	10.063	39.738
Y pol.	CryoSat	-44.277	-11.090	0.070	11.036	44.224
Y pol.	GOCE	-48.264	-12.029	0.026	12.127	48.361
Z pol.	Swarm A	-22.381	-5.438	-0.039	5.857	22.800
Z pol.	Swarm B	-20.801	-5.005	0.106	5.526	21.321
Z pol.	Swarm C	-22.494	-5.578	-0.168	5.700	22.616
Z pol.	CHAMP	-24.783	-6.110	-0.251	6.339	25.012
Z pol.	CryoSat	-24.398	-5.840	0.211	6.533	25.091
Z pol.	GOCE	-41.699	-10.351	-0.058	10.547	41.895



Table 4: Satellite and observatory bias and sigmas of the last iteration of the short period Mag . num parent model, otherwise same as in table 2.

Type in 1	Number in 1	Bias in nT	Sigma in nT
1	1527875	0.062	2.882
-1	1278565	0.118	3.018
2	1527875	0.017	2.945
-2	1278565	0.056	2.933
3	1527875	0.175	4.182
-3	1278565	-0.782	4.213
11	4278421	-0.705	43.777
-11	488	-0.353	7.590
12	4278421	0.590	51.759
-12	488	-1.110	7.519
13	4278421	-0.186	16.655
-13	488	0.281	5.716

Table 5: The statistics of the last iteration for the short period Mag . num parent model are specified here, but as result of the R standard `boxplot` command, otherwise like table 3.

Type	Source	Lower Whisker in nT	Lower Hinge in nT	Median in nT	Upper Hinge in nT	Upper Whisker in nT
X equ.	Swarm A	-6.094	-1.483	0.026	1.590	6.201
X equ.	Swarm B	-5.883	-1.355	0.115	1.664	6.192
X equ.	Swarm C	-6.233	-1.560	-0.015	1.556	6.229
Y equ.	Swarm A	-5.661	-1.451	-0.040	1.356	5.567
Y equ.	Swarm B	-5.277	-1.236	0.107	1.458	5.499
Y equ.	Swarm C	-5.681	-1.461	-0.034	1.353	5.573
Z equ.	Swarm A	-8.851	-2.344	-0.070	1.994	8.501
Z equ.	Swarm B	-8.079	-1.511	0.607	2.868	9.437
Z equ.	Swarm C	-8.820	-2.276	0.014	2.086	8.630
X pol.	Swarm A	-40.758	-10.489	0.124	9.690	39.960
X pol.	Swarm B	-40.054	-10.231	0.136	9.651	39.473
X pol.	Swarm C	-40.956	-10.534	0.156	9.748	40.170
Y pol.	Swarm A	-42.109	-10.219	0.179	11.041	42.930
Y pol.	Swarm B	-41.988	-10.338	0.102	10.761	42.411
Y pol.	Swarm C	-42.385	-10.311	0.128	11.071	43.145
Z pol.	Swarm A	-21.942	-5.385	0.009	5.654	22.211
Z pol.	Swarm B	-20.571	-5.030	0.081	5.331	20.872
Z pol.	Swarm C	-22.072	-5.525	-0.106	5.506	22.053

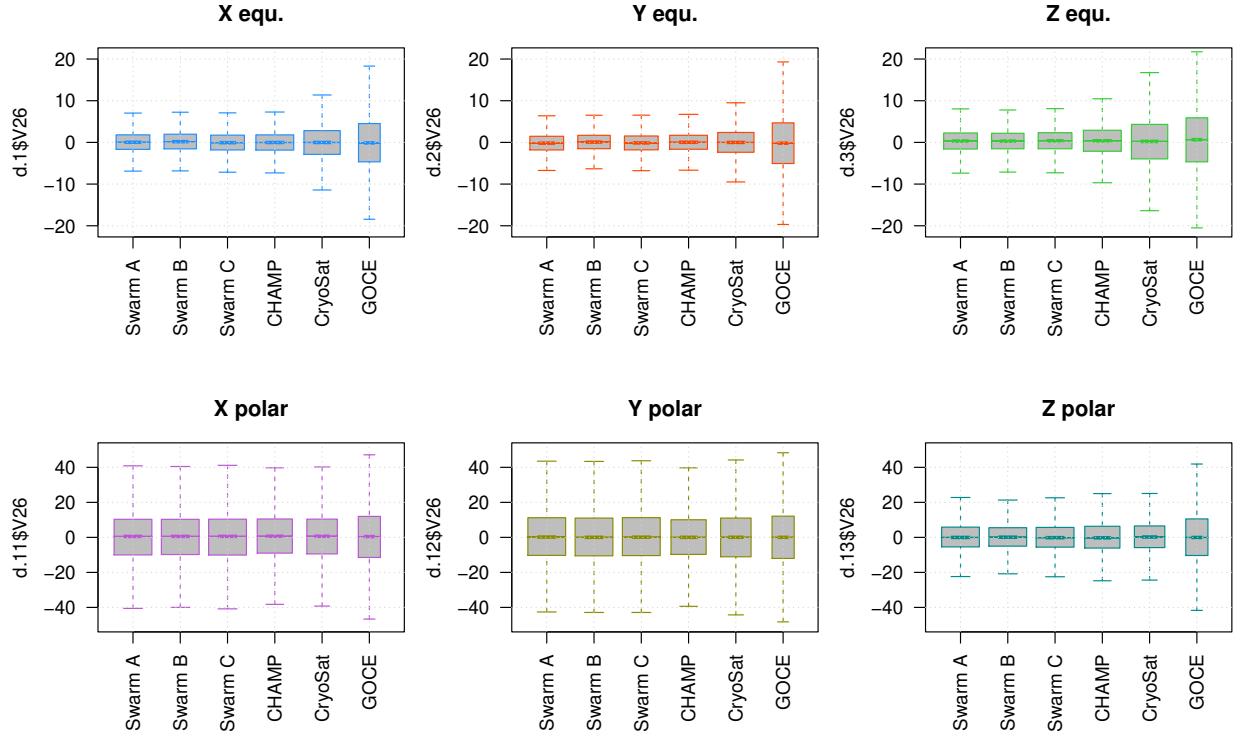


Figure 1: Whisker/Box figure corresponding to table 3 for the last iteration of the long period parent  $\text{Mag.num}$  model.

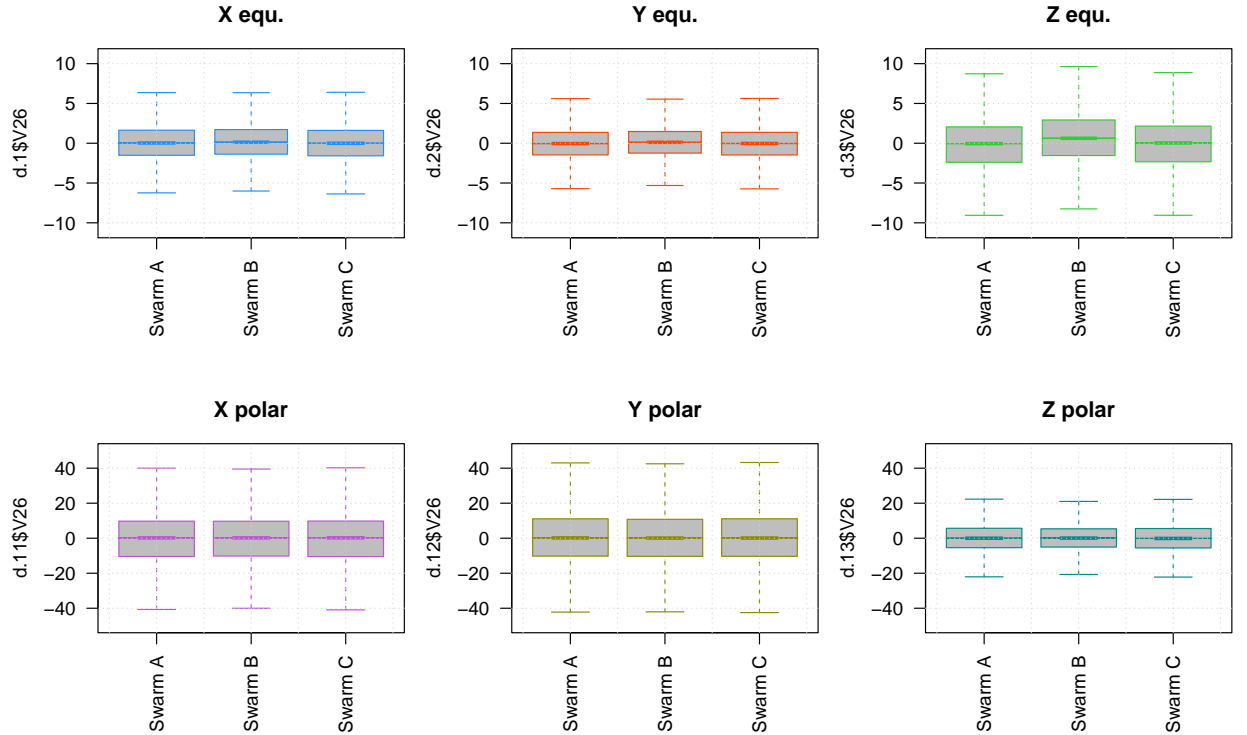


Figure 2: Whisker/Box figure corresponding to table 5 for the last iteration of the short period parent  $\text{Mag.num}$  model. Be aware of the reduced scale in the equatorial case (upper row), but detected outliers detected by the graphic routine are skipped.

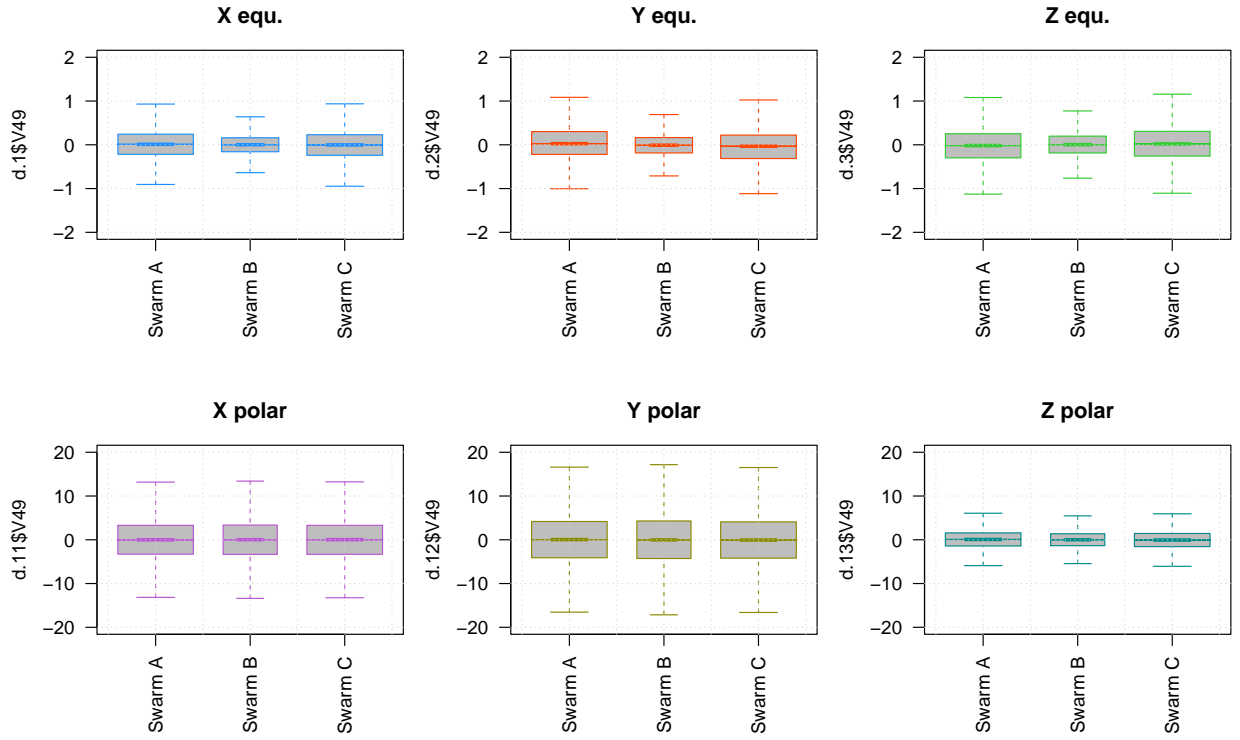


Figure 3: Whisker/Box figure corresponding to table 5 for a short model from delta data only. Be ware of the much smaller scales for the residuals, but that again detected outliers detected by the graphic routine are skipped.

## 2.8 Node and data layout

There are three model variants involved: (for the satellite data limits see Table 1.)

1. Long period `Mag.num` models, starting at epoch 2000 (with `MJD2000 0.250`) by half year (182.625 days) node steps until the end of year 2024 (approx. epoch 2025, `MJD2000 9131.500`). This model uses Swarm, CHAMP, Cryosat and GOCE satellite data and one-hourly observatory data from `AUX_OBS` product provided by BGS.
2. Short period (classic) `Mag.num` models, starting at epoch 2013 (`MJD2000 4748.500`), with the same node step size as the long model. The end epoch is also the same as for the long period model and Swarm satellite 1 Hz data is used, both with and without the `AUX_OBS` observatory data.
3. Short period delta data only models, with the same node layout as the classical short `Mag.num` model. The input data is the same as for the classical model. To ease the procedure, the data is taken from an internal data base, which is a copy of the vectors from the ESA server. This data requires an additional ex post selection step: some *far* outliers in the residuals are removed by residual thresholds *before* the first iteration, using a raw initial model.

## 2.9 Forecasts

There are two predictions required:

1. For the `IGRF` a prediction to the end of the year 2024 has to be performed.
2. For the `IGRF SV`, covering the next five years, an evaluation at the mid-node of the year 2027 (epoch 2027.5) is required.

The intended machine learning attempts, unfortunately, did not work out as expected. Either they gave unreasonable results or they had to be terminated due to excessively long computation times of two weeks without identifiable progress. To hold the `IGRF` delivery deadline, the tested fallback solution was applied for both cases (`IGRF` and `IGRF SV`), using the `forecast` library from R scripting language library. The chosen forecasting algorithm is `burg`, with disabled automatic parameter tuning. This approach was tested on the case of the last `IGRF-13` and was presented at `IUGG Juli 2023` in Berlin (A21b `IUGG23-1870`). The `IGRF SV` forecast is much more fragile than the `IGRF` forecast, as it covers several years in contrast to a few month.

## 2.10 Data misfit and residuals

The resulting residuals are calculated for the selected and later slightly filtered data as input for the modelling process.

For biases and misfits of the last iteration of the **long** period model see tables 1 and 3. The values are un-weighted estimates, and therefore can be strongly affected by outliers. Additional to the modified Huber norm (see *Lesur et al.* [2014]) used for the final iterations of the short period `Mag.num` models, the influence of far outliers was reduced a bit by threshold filtering.

For comparison, see the corresponding short model in Fig.2.

## 3 DGRF 2020 candidate

The `DGRF GFZ` candidate is calculated as the mean of a selection of the 20 models shown in table 6. The selection was performed based on consistency of the corresponding `IGRF` prediction. First, snapshots at 2020.0 and forecasts to 2025.0 are calculated for each model. Then, the mean of all 20 model `IGRF` predictions was calculated. Models for which any coefficient deviated more than 5 nT from the mean are removed from the selection. This way, 5 of the 20 models were excluded (models 2, 4, 9, 10 and 19). The model deviations and selection are depicted in figure 5. The mean of the remaining models is our candidate for both `DGRF 2020` and `IGRF 2025`. The standard deviations of the cleaned selection are reported as uncertainties.

In comparison to older `IGRF` candidates from the `GRIMM` family, the additional satellite data from `GOCE` and `CryoSat` stabilized the model during the gap period between `CHAMP` and `SWARM`. The additional data are limited to cover the gap with only a moderate, arbitrarily chosen overlap (see figure 4). For the epoch 2020 this was not pivotal.

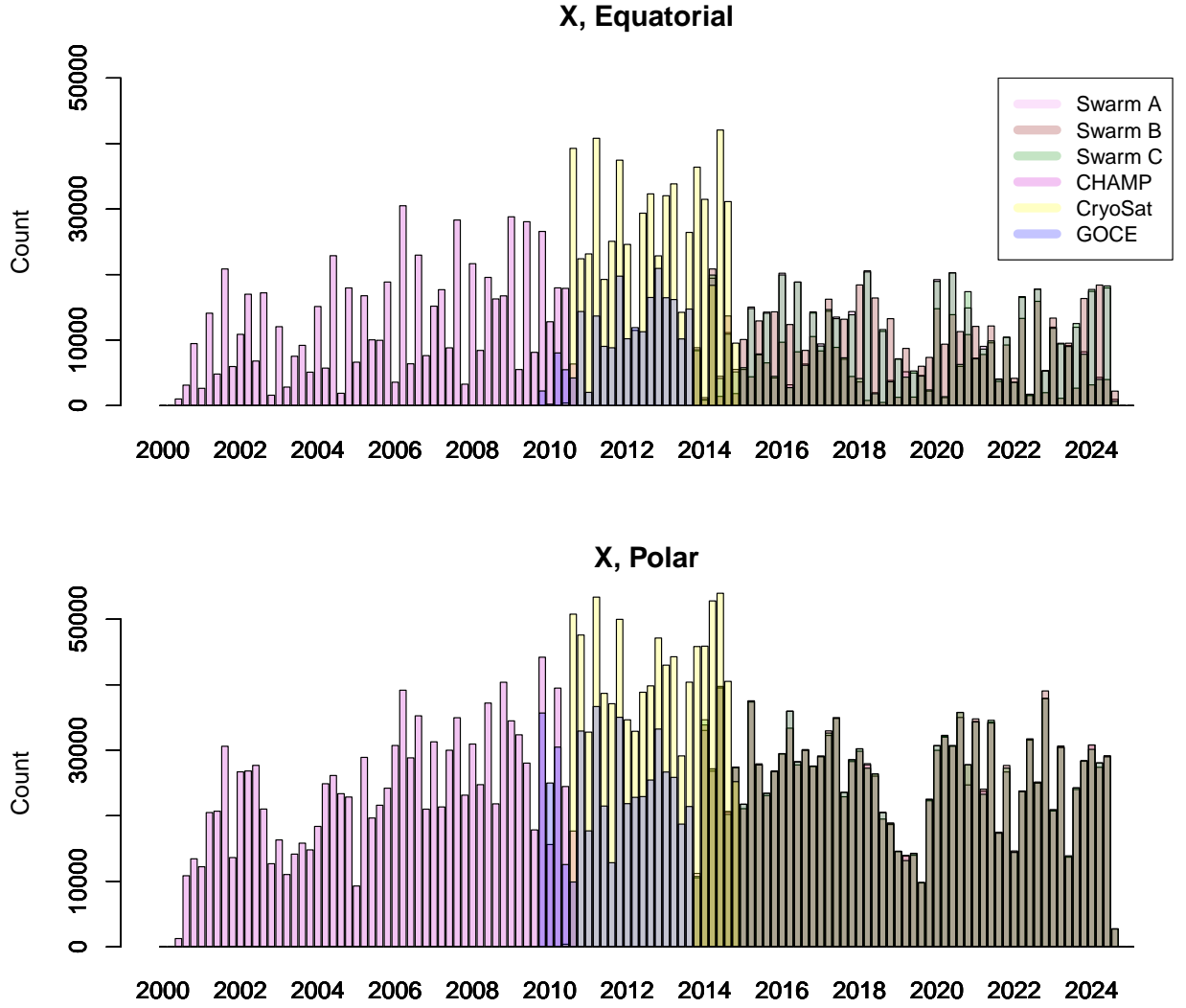


Figure 4: Data coverage for the long-period  $\text{Mag.num}$  model over Years. The gap between CHAMP and Swarm mission is bridged by GOCE and CryoSat readings. See also table 1.

In addition to the multiple long term models, several shorter models are available, each with dedicated different features: Short models with and without observatory data and models built from delta-data only. The delta only models are likely less affected by large scale external field contributions. See Table 6 for a compact overview.

## 4 IGRF-2025 candidate

For each of the 20 reasonable models available (table 6) forecasts to epoch 2025 are done with the AR method. The end-period for the data used for forecasting is limited to epoch 2024.5, as this node is still well covered by Swarm data. Our IGRF 2025 candidate is calculated as the mean of a selection of the 20 forecasts. See the previous section for details.

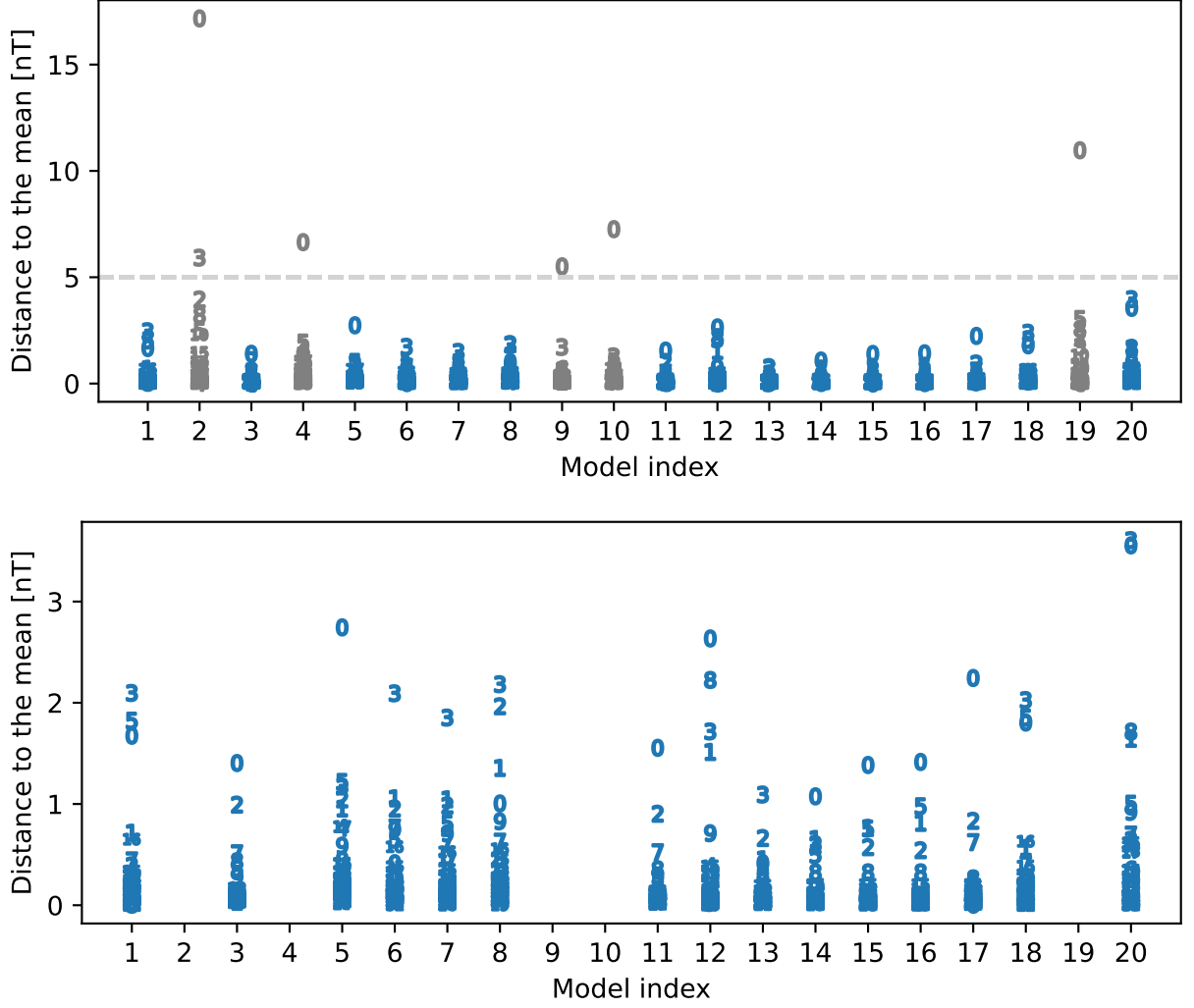


Figure 5: Deviance of the individual IGRF model coefficients from the ensemble mean, before (top) and after (bottom) model selection. Grey models in the top panel are removed from the ensemble, as they are above the threshold (dashed line). The numbers refer to the spherical harmonics index, i.e. 0 is  $g_1^0$ , 2 is  $h_1^1$ , 3 is  $g_2^0$  etc.

Table 6: Set of models internal number and type, used for a candidate type or removed from set by deviance. See Figures 5 and 7.

Index	Model Type	Used for
1	Long	DGRF, IGRF, SV
2	Long	none
3	Short	DGRF, IGRF, SV
4	Short, Delta	none
5	Short, Delta	DGRF, IGRF, SV
6	Short, Delta	DGRF, IGRF, SV
7	Short, Delta	DGRF, IGRF, SV
8	Short, Delta	DGRF, IGRF, SV
9	Short, Delta	SV
10	Short, Delta	none
11	Short	DGRF, IGRF, SV
12	Short	DGRF, IGRF
13	Short	DGRF, IGRF, SV
14	Short	DGRF, IGRF, SV
15	Short	DGRF, IGRF, SV
16	Short	DGRF, IGRF, SV
17	Short	DGRF, IGRF, SV
18	Long	DGRF, IGRF, SV
19	Long	SV
20	Long	DGRF, IGRF, SV

## 5 IGRF SV candidate

The approach for calculating our IGRF SV candidates is similar to the method for calculating the IGRF 2025 candidate. However, a forecast to the epoch 2030.0 appears to overextend the AR method, as seen from a strong curvature in the forecast curves. To prevent this, we limit the forecast to the epoch 2027.5 and also limit the used model period for forecasting to epoch 2024.0. This may reduce the influence of the uncovered final node without a need for additional model damping. Again, forecasts are created for each of the 20 models in the set (table 6). The model forecast is in general not a straight line. To reduce the forecast to a single, linear SV information, a robust linear fit (`rlm` routine from R library `MASS`) is applied to the period for each coefficient. The intercept part is ignored and the estimated slope is used as SV for the particular model from the set. This way, 20 SV candidates are produced. Fig. 6 shows the forecast period and the line fit for a single long period model (index 2 in table 6). This model shows unexpected behaviour and has been dropped by the threshold criterion.

From the ensemble we proceed similar to the DGRF 2020 and IGRF 2025 candidates. First the mean SV is calculated. Then, models 2, 4, 10 and 12 are removed, as they deviate more than 6 nT/yr. from the mean. The threshold is slightly larger than for the IGRF, as the secular variation is less well constrained. The mean of the remaining 16 models is our IGRF SV candidate and the ensemble standard deviation is reported as uncertainties. The model selection is depicted in figure 7

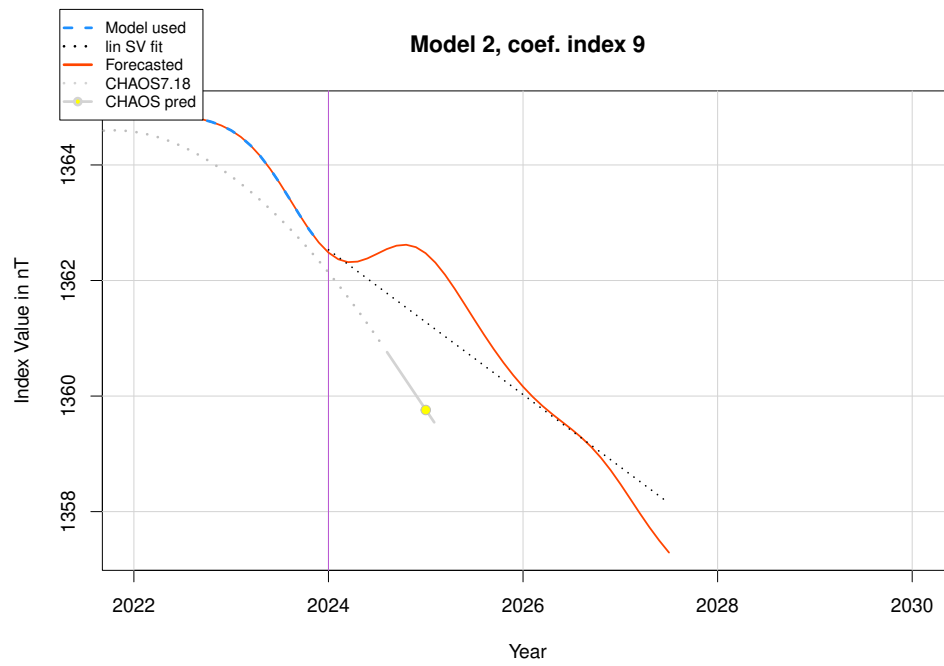


Figure 6: Example case (coefficient index 9 of Model 2) for a forecast and the line fitted; this model was excluded by threshold limit from the candidate estimations.



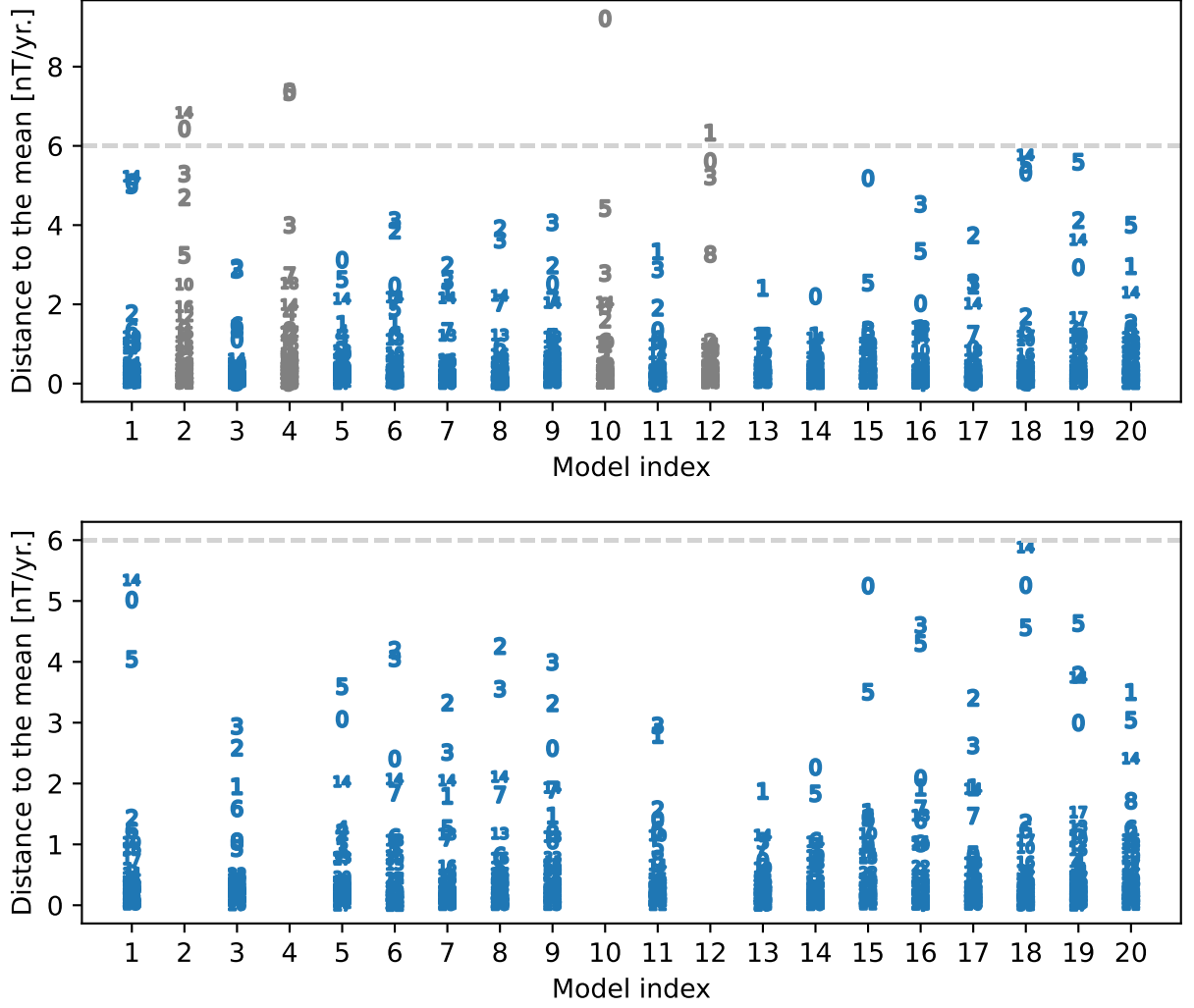


Figure 7: Deviance of the individual IGRF SV model coefficients from the ensemble mean, before (top) and after (bottom) model selection. Grey models in the top panel are removed from the ensemble, as they are above the threshold (dashed line). The numbers refer to the spherical harmonics index, i.e. 0 is  $g_1^0$ , 2 is  $h_1^1$ , 3 is  $g_2^0$  etc.

## References

- Lesur, V., I. Wardinski, M. Rother, and M. Manda, GRIMM: the GFZ Reference Internal Magnetic Model based on vector satellite and observatory data, *Geophysical Journal International*, 173, 382–394, doi:10.1111/j.1365-246X.2008.03724.x, 2008.
- Lesur, V., N. Olsen, and A. Thomson, *Geomagnetic Core Field Models in the Satellite Era*, vol. 5, chap. 11, pp. 277–294, Springer, doi:10.1007/978-90-481-9858-0, 2010.
- Lesur, V., M. Rother, I. Wardinski, R. Schachtschneider, M. Hamoudi, and A. Chambodut, IGRF-12 GFZ candidates, *techreport*, Helmholtz Centre Potsdam, GFZ German Research centre for Geosciences, 2014.
- Macmillan, S., and N. Olsen, Observatory data and the Swarm mission, *Earth, Planets and Space*, 65(11), 1355–1362, doi:10.5047/eps.2013.07.011, 2013.
- Manda, M., I. Panet, V. Lesur, O. De Viron, and M. Diamant, The earth’s fluid core: recent changes derived from space observations of geopotential fields, *PNAS*, doi: 10.1073/pnas.1207346109, 2012.
- Olsen, N., G. Albin, J. Bouffard, T. Parrinello, and L. Tøffner-Clausen, Magnetic observations from CryoSat-2: calibration and processing of satellite platform magnetometer data, *Earth Planets and Space*, (72), doi:10.1186/s40623-020-01171-9, 2020.
- Rother, M., and I. Michaelis, CH-ME-3-MAG - CHAMP 1 Hz Combined Magnetic Field Time Series (Level 3), *Tech. rep.*, GFZ Data Services, doi: doi.org/10.5880/GFZ.2.3.2019.004, 2019.
- Rother, M., V. Lesur, and R. Schachtschneider, An algorithm for deriving core magnetic field models from the swarm data set, *Earth Plan. Spa.*, 65, 1223–1231, doi: 10.5047/eps.2013.07.005, 2013.
- Styp-Rekowski, K., I. Michaelis, C. Stolle, J. Baerenzung, M. Korte, and O. Kao, GOCE ML-calibrated magnetic field data. V. 0301, *Tech. rep.*, GFZ Data Services, doi: doi.org/10.5880/GFZ.2.3.2022.002, 2022.